Biaxial shear of confined colloidal hard spheres: the structure and rheology of the vorticity-aligned string phase†

Neil Y. C. Lin,* Xiang Cheng‡ and Itai Cohen

Using a novel biaxial confocal rheoscope, we investigate the flow of the shear induced vorticity aligned string phase [X. Cheng *et al.*, *Proc. Natl. Acad. Sci. U. S. A.*, 2011, **109**, 63], which has a highly anisotropic microstructure. Using biaxial shear protocols we show that we have excellent control of the string phase anisotropic morphology. We choose a shear protocol that drives the system into the string phase. Subsequently, a biaxial force measurement device is used to determine the suspension rheology along both the flow and vorticity directions. We find no measurable dependence of the suspension stress response along the shear and vorticity directions due to the hydrodynamically induced string morphology. In particular, we find that the suspension's high frequency stress response is nearly identical along the two orthogonal directions. While we do observe an anisotropic stress response at lower shear frequencies associated with shear thinning, we show that this anisotropy is independent of the shear induced string structure. These results suggest that for the range of flows explored, Brownian and hydrodynamic contributions to the stress arising from the anisotropic suspension microstructure are sufficiently weak that they do not significantly contribute to the rheology. Collectively, this study presents a general and powerful approach for using biaxial confocal rheometry to elucidate the relationship between microstructure and rheology in complex fluids driven far-from-equilibrium.

1 Introduction

Anisotropic materials are ubiquitous in nature – examples include wood, bone,[1] anisotropic crystals,[2,3] and plasmas.[4] Furthermore, many soft materials, which are important for industrial and biological applications, form anisotropic structures in response to external fields[5,6] and demonstrate highly anisotropic viscosities. Representative examples include nematic liquid crystals,[7,8] magnetic fluids,[9] and muscle tissues,[10] all of which exhibit different viscosities along different directions. In many of these systems, anisotropic microstructures give rise to the anisotropic mechanical properties.

A particularly striking example of anisotropic microstructures are the various vorticity-aligned assemblies found in many complex fluids, including thixotropic clay gels,[11] attractive colloids[12] and emulsion droplets,[13] nanotube suspensions,[14–16] fiber suspensions,[17] and hard sphere colloids.[18] Such phases are of technological interest since they have potential applications in the areas of nano-fabrication and bio-analysis.[19–21] Despite

extensive study of these shear induced anisotropic structures and their rheology under uniaxial shear,[12–18] the relation between the structures they form and their corresponding direction-dependent viscosities is still poorly explored. One of the technical hurdles for relating anisotropic structure to the material's anisotropic rheology is the inability to simultaneously image the sample microstructure while measuring its anisotropic rheology.

Here, we use a newly developed technique to simultaneously investigate the structure and biaxial rheology of the vorticity-aligned string phase in sheared colloidal suspensions under confinement. This phase demonstrates string-like particle assemblies aligning along the vorticity direction, and has a one-dimensional translational symmetry.[12,18,22–26] In many systems it has been suggested that the vorticity-aligned structures arise from interparticle attractions.[12–14,16] In contrast, the string assemblies in the hard sphere colloid system investigated here, result from the unique interactions that arise from geometric constraint and hydrodynamic particle–particle and particle-wall couplings all of which are enhanced by confinement.[18]

To measure suspension rheology we construct a biaxial confocal rheoscope by combining a dual-directional shear cell with a biaxial force measurement device. This apparatus allows for manipulating the formation and the orientation of shear-induced structures while simultaneously measuring their anisotropic mechanical response, and imaging their

Department of Physics, Cornell University, Ithaca, New York 14853, USA. E-mail: yl834@cornell.edu

‡ Present address: Department of Chemical Engineering and Materials Science, University of Minnesota, Minneapolis, Minnesota 55455, USA.

structure.[27–31] We first demonstrate direct control over the isotropic-to-string phase transition using biaxial shear flows. With this technique in conjunction with *oscillatory superposition spectroscopy*, we then directly measure the rheology of the string phase along different directions. Surprisingly, we find that the anisotropic structure has a negligible effect on the corresponding rheological properties of the suspension.

2 Experimental method

The schematic of the biaxial shear cell is illustrated in Fig. 1. For each experimental run, 10 µl of suspension are loaded in a gap consisting of a coverslip and a 4 mm × 4 mm silicon wafer with a 9 µm separation between them. Both plates are adjusted to be parallel within 0.0075° by turning three set screws. The coverslip is coupled to a multi-axis piezo (PI P-733) that can generate movements along all directions to apply biaxial shear flows. The silicon wafer is attached to a biaxial force measurement device (FMD) so that the shear stresses σ_{xy} and σ_{zy} are measured simultaneously. Here, X, Y, and Z correspond to the flow, gradient, and vorticity axes of the first shear flow.

In the FMD, eight foil gauges – four for each direction – are wired as two independent Wheatstone bridges that enable stress measurement. All signals measured by the FMD are amplified by signal conditioning amplifiers (Vishay 2310B) then digitized for Fourier analysis. By mounting this biaxial shear cell on a fast confocal microscope (Zeiss LSM 5 Live), we also image the microstructure while the suspension is sheared and the stress response is measured. The calibration details of the shear cell alignment and the FMD performance are in the Appendix.

Our sample is comprised of silica particles with diameter $a = 1.3$ µm suspended in a 1 : 4 water–glycerin mixture. The solvent has a viscosity $\eta = 0.06$ Pa s and a refractive index of 1.442 that matches that of the particles. The suspension volume fractions

we work with are $\phi = 0.37$ and 0.47. We add 1.25 mg ml^{-1} of fluorescein sodium salt to dye the solvent for confocal imaging. The electrostatic screening length is ∼10 nm, so that the interparticle interactions are nearly hard-sphere.

The biaxial shear flow imposed can be divided into two oscillatory shear flows

$$\overline{\overline{\gamma}}(t) = \overline{\overline{\gamma}}_1 \sin(\omega_1 t) + \overline{\overline{\gamma}}_2 \sin(\omega_2 t + \delta_\gamma). \tag{1}$$

Here, $\overline{\overline{\gamma}}$ corresponds to the strain amplitude tensor, ω corresponds to the shear frequency, and δ_γ corresponds to the phase angle difference between the first flow, indicated by the subscript 1 and the second flow, indicated by the subscript 2. When both the first and the second flows are parallel, the strains $\overline{\overline{\gamma}}_1$ and $\overline{\overline{\gamma}}_2$ are aligned and the stress response is probed along the flow direction. When the first and the second flows are perpendicular, the strain $\overline{\overline{\gamma}}_2$ probes the response orthogonal to the direction of the first flow.

3 2D-oscillatory shear: phase angle dependence of structure and rheology

In the phase angle experiment, we set the first flow $\overline{\overline{\gamma}}_1 = 2.50\hat{X}\hat{Y}$ and the second flow $\overline{\overline{\gamma}}_2 = 2.50\hat{Z}\hat{Y}$ perpendicular. Here, while the flows characterized by γ_1 and γ_2 are along X-axis and Z-axis respectively, both γ_1 and γ_2 share the same gradient axis (Y-axis). We fix the shear frequency at $\omega_1 = \omega_2 = 31.4$ s^{-1} and vary the phase angle δ_γ over the range $0 \leq \delta_\gamma \leq \pi$. Thus the maximum shear rate along each axis is 78.5 s^{-1}, which corresponds to Pe = 4.73×10^3. Here, the Péclet number is defined as Pe = $6\pi\eta_0\dot{\gamma}a^3/(8k_BT)$ and characterizes the ratio of the shear rate $\dot{\gamma}$ to the relaxation rate $1/\tau_s$ of the sample. This method has been introduced as 2D-SAOS (small amplitude oscillatory shear) when the strain amplitude ($\leq 5 \times 10^{-2}$) is small.[32]

Fig. 2(a)–(c) show the normalized magnitude $\tilde{\gamma}_1$ *versus* $\tilde{\gamma}_2$ Lissajous-Bowditch curves for the imposed flows where $\delta_\gamma = 0$, $\pi/6$ and $\pi/2$ respectively. For $\delta_\gamma = 0$, the shear strain trajectory is linear and aligned at 45° to the X-axis. This linearly polarized shear flow is the same as the uniaxial shear flow with a different orientation (Fig. 2(a)). In Fig. 2(b) and (c), $\overline{\overline{\gamma}}(t)$ is elliptically polarized with $\delta_\gamma = \pi/6$ and circularly polarized with $\delta_\gamma = \pi/2$.

Previous measurements have shown that the string structures are most pronounced near the boundaries.[18] Thus, for each phase angle, we image the colloidal particles in the second layer 2.5 µm below the top stationary plate. We find that as δ_γ changes from 0 to $\pi/2$ the suspension structure transitions from a string morphology to one that is isotropic (Fig. 2(d–f)). To illustrate this transition we calculate the pair correlation functions $g(\vec{r})$ and average them individually over 20 cycles of shear (Fig. 2(g)–(i)). Here $g(\vec{r})$ is the normalized probability of finding a particle at vector $\vec{r}$ with respect to another particle in the X–Z plane. In Fig. 2(d), we find that when the suspension is subjected to a linearly polarized shear flow, $g(\vec{r})$ demonstrates a highly anisotropic distribution at its first peak and exhibits stripes at larger $\vec{r}$. These stripes along with the anisotropic distribution of particle densities confirm that particles align along the vorticity direction and form string structures under
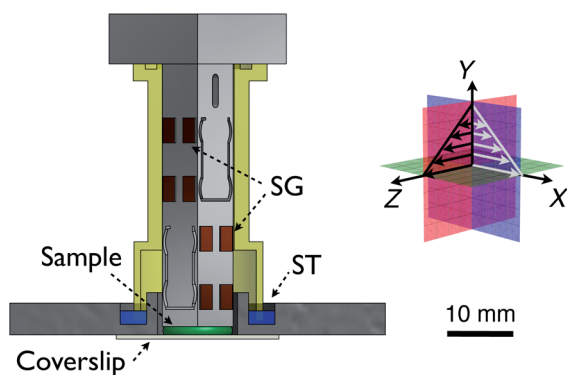

Fig. 1   Three dimensional schematic of the biaxial force measurement device (left) and coordinate definition (right). The abbreviations SG and ST stand for strain gauges and the solvent trap, respectively. The lower strain gauges measure the stress response along the X-axis, σ_{xy}, and the upper ones measure the response along the Z-axis, σ_{zy}. The gap between the top plate (silicone wafer) and the bottom plate (coverslip) is exaggerated for clarity. The gap separation in the experiments is 9.0 µm. The shear flow is separately imposed along the X and Z axes by moving the bottom plate using a multi-axis piezoelectric actuator.
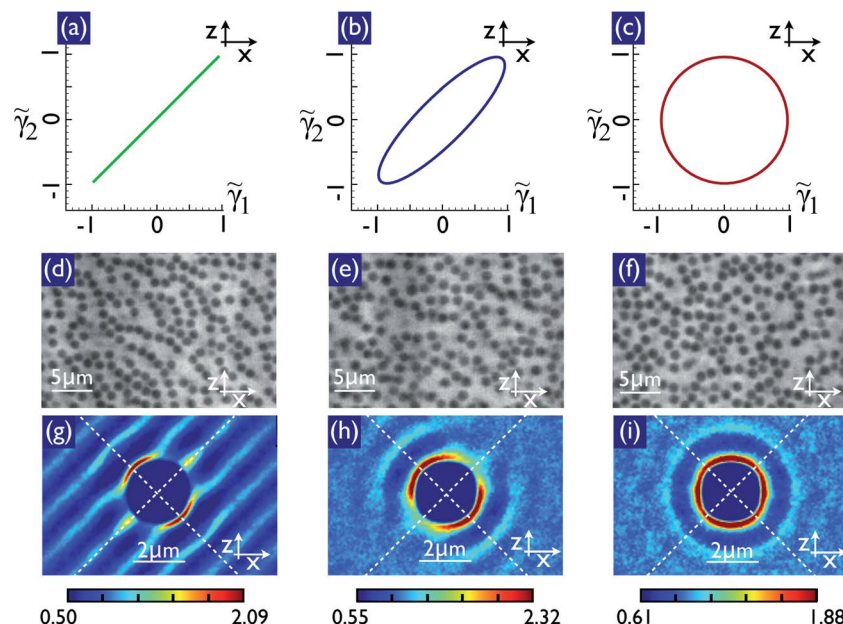
Fig. 2 Suspension microstructure for three phase angles $\delta_\gamma = 0$, $\pi/6$ and $\pi/2$. Lissajous curves for the normalized shear strains $\tilde{\gamma}_y$ versus $\tilde{\gamma}_x$ are plotted in (a)–(c), where (a)–(c) correspond to $\delta_\gamma = 0$, $\pi/6$ and $\pi/2$ respectively. The 2D confocal images of the suspension with $\delta_\gamma = 0$, $\pi/6$ and $\pi/2$ are shown in (d)–(f) respectively. The corresponding pair correlation functions $g(\vec{r})$ of the particle distribution are shown in (g)–(i). Each $g(\vec{r})$ image represents a measurement averaged over 20 shear cycles. The dashed lines are guides for the eye and denote the 45° and the 135° orientations. The color ranges in the density plots are chosen to emphasize the structural features.

uniaxial shear (Fig. 2(g)). This finding is consistent with previous results.[18] As δ_γ increases to $\pi/6$, the first peak of $g(\vec{r})$ maintains a similar shape but with a broader peak width. Most stripes disappear and the anisotropy of the second and the third peaks of $g(\vec{r})$ significantly decreases (Fig. 2(h)). Finally, for $\delta_\gamma = \pi/2$, $g(\vec{r})$ is isotropic indicating that the suspension is characterized by liquid-like order Fig. 2(i).

Additional structural characterization of the string phase including the alignment order parameter, layering, and time dependence can be found in (ESI†). Here we simply point out that by imposing different phase angles we are able to control the suspension structure while keeping the Pe for the flows along both axes constant. This protocol allows for excluding effects from other contributions, including Brownian stresses and hydrodynamic coupling, that can arise when comparing the rheology of the sample at different shear rates.

Using this protocol we study the relation between the rheology and the anisotropic microstructure by measuring the stress responses along the X-axis, σ_{xy}, and the Z-axis, σ_{zy}, simultaneously for different phase angles δ_γ. We find that the first harmonic term for the stress response accounts for over 90% of the force amplitude and dominates the higher order terms,[33] which are often buried in the noise. We therefore report the first harmonic response amplitude as the measured stress peak within one shear cycle. We plot σ_{xy} and σ_{zy} versus δ_γ in Fig. 3(a). Despite the dramatic change in microstructure, we find that both σ_{xy} and σ_{zy} are independent of δ_γ. To measure the Pe-dependence of stress responses we perform an amplitude sweep over the range $5.70 \times 10^{-3} \leq |\bar{\gamma}| \leq 3.00$ while keeping the frequencies fixed at 31.4 s^{-1}. We plot σ_{xy} versus Péclet number

for both $\delta_\gamma = 0$ (linear) and $\delta_\gamma = \pi/2$ (circular) polarizations in Fig. 3(b). We find quantitatively similar dependencies for both polarizations. These data indicate that for $\omega = 31.4$ s^{-1} the shear induced in-plane structure does not alter the suspension rheology for $11 < \text{Pe} < 5.7 \times 10^3$.

4 Oscillatory superposition spectroscopy

To probe the anisotropic rheological properties of the suspensions, we perform an *oscillatory superposition spectroscopy* measurement.[34,35] Similar methods have recently gained traction for determining the shear thinning behavior of polymer solutions[34,35] and colloidal glasses,[36,37] as well as slow relaxations in granular systems.[38] To investigate the string phase we choose the first shear flow along the X-axis that generates the most pronounced strings ($|\bar{\bar{\gamma}}_1| = 2.50$ and $\omega = 31.4$ s^{-1}), and use the second flow to probe the suspension response. It is important to note that in such biaxial flow experiments, technically there are no well defined vorticity and flow axes for the overall flow, as shear is being applied in both the X–Y and Z–Y planes. Nevertheless, it is still useful to think of the system as being driven by the first flow and being probed by the second flow. These labels do however lose their meaning as the shear rate due to the second flow becomes comparable to that of the first flow.

Because the rheological phase space that can be explored is vast and because the measurements are time intensive, we use the second flow to conduct an amplitude and a frequency
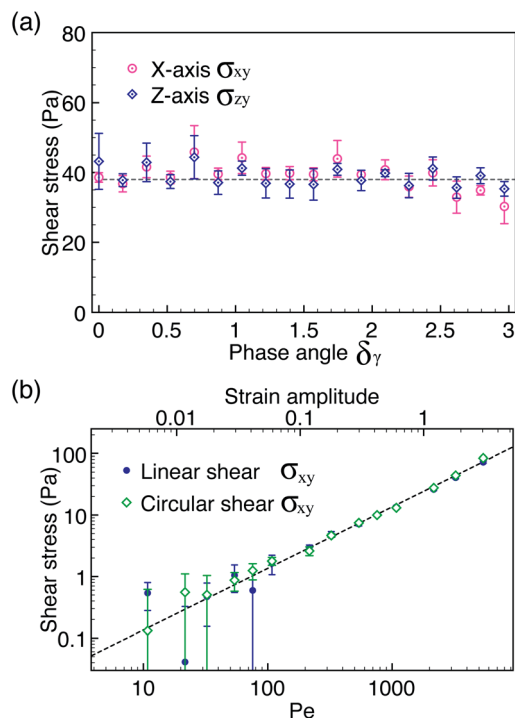
Fig. 3 Suspension stress response *versus* δ_γ (a) and Pe (b). (a) The stress responses along the *X*-axis, σ_{xy}, and the *Z*-axis, σ_{zy}, are plotted *versus* δ_γ with $\gamma_{1,2} = 2.50$ and $\omega_{1,2} = 31.4 \text{ s}^{-1}$. The dashed horizontal line indicates the mean value of the data. Each data point is averaged over five independent measurement runs with each run consisting of 500 cycles. (b) The stress response is plotted as a function of Pe for linearly polarized and circularly polarized shear flows. The data are consistent with a Newtonian response as indicated by the linear fit (dashed line). We note that the smallest measureable stress difference would correspond to approximately twice the error bar value or ~10 Pa.
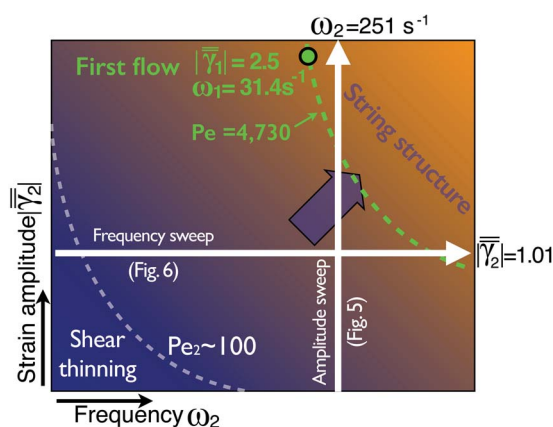

Fig. 4 Pipkin diagram of the explored regime in this experiment. The green dashed curve denotes the constant Pe of the first flow. The gray dashed curve indicates the shear thinning regime. Two long arrows illustrate the amplitude (vertical) and frequency (horizontal) sweep measurements performed.

sweep. These measurements are able to investigate the string phase rheology over a range of flow rates that separately capture the hydrodynamic and Brownian contributions to the stress

response. The regime of the string structure rheology that these measurements access is illustrated in the Pipkin diagram in Fig. 4.

4.1 Amplitude sweep: hydrodynamic contributions

In the amplitude sweep measurements, we conduct experiments using parallel and orthogonal modulations of the first shear flow. In both orthogonal and parallel cases we record the total stress for 500 cycles and then take a Fourier transform of the measurement to read out the response – σ_{zy}, or σ_{xy} at the frequency ω_2. The regime examined by this measurement is depicted by the vertical white arrow in Fig. 4. We plot $\sigma_{zy}(\omega_2)$ for the orthogonal modulation (green diamonds) and $\sigma_{xy}(\omega_2)$ for the parallel modulation (blue squares) *versus* Pe_2 (bottom axis) and $|\overline{\overline{\gamma}}_2|$ (upper axis) in Fig. 5(a). We find that the measurements for both modulations are quantitatively similar. In both
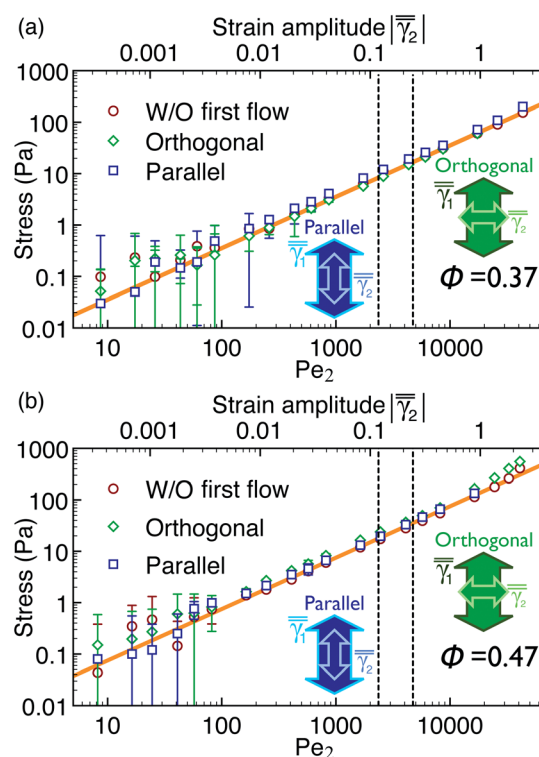

Fig. 5 Stress responses measured using oscillatory superposition spectroscopy for orthogonal (green diamonds) and parallel modulations (blue squares). (a) Stresses measured in the modulation experiments are plotted as a function of Pe_2 for $\phi = 0.37$. The stress response without the first flow is also shown in the plot for comparison (red circles). The dashed vertical lines are the first flow Péclet numbers for orthogonal (right) and parallel (left). The oblique dashed line is the theoretical calculation of the hydrodynamic stress response.[39] In the parallel modulation experiment, Pe_1 is smaller than that of orthogonal modulation due to the limitation of the piezo travel distance. (b) Stress measurements with the same shear protocols conducted for a denser suspension with $\phi = 0.47$. This suspension demonstrates a slight shear thickening behavior when $\text{Pe}_2 \gtrsim 10^4$. The orange lines in both figures are the theoretical values for the hydrodynamic stress response calculated using eqn (2).[39] The smallest measureable stress difference in the amplitude sweep measurements would correspond to approximately twice the error bar value or ~1 Pa.

cases we find a linear dependence of stress on Pe_2 indicating a Newtonian response. Thus, we find no measurable effect of the string structure on the suspension oscillatory shear rheology. To further probe the dependence of rheology on the shear induced string structure we conduct additional experiments in which the first flow is absent (red circles). We find that the stress measurements for these flows are quantitatively similar to those in which the first flow is applied. Collectively these results demonstrate that despite the formation of string structures, the suspension response remains isotropic. In addition, we calculate the hydrodynamically dominated high frequency stress response for an isotropic bulk suspension[39] with $\phi = 0.37$ using

$$\eta_H = \frac{1 + \frac{3}{2}\phi\left[1 + \phi\left(1 + \phi - 2.3\phi^2\right)\right]}{1 - \phi\left[1 + \phi\left(1 + \phi - 2.3\phi^2\right)\right]}. \tag{2}$$

We find that the predicted viscosity $\eta_H = 240$ mPa s gives a stress response (orange lines in Fig. 5) that is in excellent agreement with the data. We also find that the suspension stress response remains linear in the applied strain amplitude at low $Pe \leq 100$ and small amplitudes $|\overline{\overline{\gamma}}_2| \leq 2.00 \times 10^{-3}$. This linear stress response results in an amplitude-independent complex viscosity magnitude,[40] which is consistent with active microrheology measurements on quiescent suspensions where the applied oscillation frequency of the probe particle exceeds the relaxation rate of the suspension.[41]

The overlap between the data and the relation from eqn (2) suggests that the tested confined suspension demonstrates a bulk stress response. We do however note that the gap height corresponds to approximately seven particle layers. Here, our goal was to maximize the portion of the suspension forming the string phase. At larger gaps strings no longer form while at smaller gaps the rheology is dominated by the suspension structures arising from interactions with the shearing plates. Thus it is difficult to test the explicit effects of confinement on the rheology of the string phase. More broadly, whether the rheology exhibits significant dependence on gap height for confined suspensions remains an interesting open question that we hope to address in future work.

To test whether these results also apply in higher volume fraction suspensions, we conduct an identical amplitude sweep measurement with a denser suspension ($\phi = 0.47$), and plot the stress responses in Fig. 5(b). The rheological properties of the denser suspension are qualitatively similar to that of the sample with an intermediate volume fraction $\phi = 0.37$ (Fig. 5(a)). In addition, no wall slip is observed at either volume fraction.[28] Overall, these results imply that for the range of Pe_2 explored, the shear stress response of the string phase is dominated by a hydrodynamic contribution that is independent of the shear induced suspension structure.

4.2 Frequency sweep: Brownian contributions

Shear thinning in suspensions results from the decreased relative contribution of the Brownian stresses to the total stress.[28,42–44] To probe whether the string structure alters the

response in the shear thinning regime we conduct a frequency sweep measurement. To confirm that we are probing the shear thinning regime we first characterize the flow behavior of quiescent suspensions where no first flows are imposed. We plot the stress response *versus* Pe_2 for $\phi = 0.37$ and 0.47 in Fig 6. Consistent with prior literature results, we find very weak shear thinning for the $\phi = 0.37$ sample (red squares) and a pronounced thinning behavior for the $\phi = 0.47$ sample (red circles).[44,45]

Next, we impose a first shear flow with $|\overline{\overline{\gamma}}_1| = 2.50$ at $Pe_1 = 4.73 \times 10^3$ that is strong enough to generate the string phase and conduct oscillatory superposition spectroscopy measurements using parallel and orthogonal modulations. For both the orthogonal and parallel modulations, we set $|\overline{\overline{\gamma}}_2| = 1.01$ and vary the frequency so that $17.2 \leq Pe_2 \leq 1.72 \times 10^4$. The regime explored by this frequency sweep measurement is depicted by the horizontal white arrow in Fig. 4.

We plot $\sigma_{zy}(\omega_2)$ for the orthogonal modulation (green squares) and $\sigma_{xy}(\omega_2)$ for the parallel modulation (blue diamonds) *versus* Pe_2 (bottom axis) and ω_2 (upper axis) in Fig. 6. The data for the intermediate ($\phi = 0.37$) and high ($\phi = 0.47$) volume fractions are denoted by the dotted and open symbols respectively. Because the shear thinning behavior is weak ($\sim$30%) for $\phi = 0.37$,[44,45] the change of the flow behavior at low Pe is barely measurable with our force measurement device. For the high volume fraction suspension ($\phi = 0.47$), we find that the stress response along the orthogonal direction (green squares) demonstrates pronounced shear thinning behavior for $Pe_2 < 200$. In contrast, we find that the stress response along the parallel direction (blue diamonds) linearly increases with Pe_2 indicating that the suspension has already been shear thinned by the first flow. We highlight this anisotropic responses by plotting the corresponding complex viscosity magnitudes $|\sigma/\dot\gamma|$ in the inset of Fig. 6.
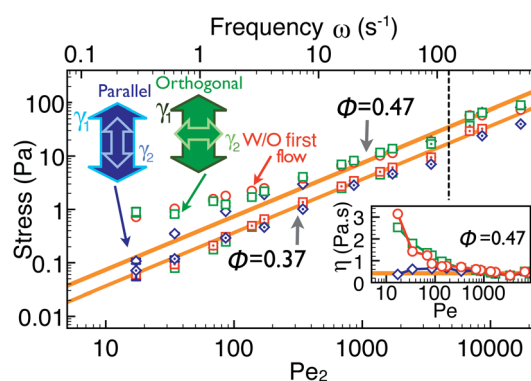

Fig. 6 Stress responses measured using frequency sweep protocols for $\phi = 0.37$ (dotted symbols) and $\phi = 0.47$ (open symbols). The data for both volume fractions share the same color code. The orange lines are the high frequency responses calculated from eqn (2). The inset shows the corresponding complex viscosity magnitudes of the suspension with $\phi = 0.47$. The error bars illustrate the standard errors of the data averaged over five runs of measurements. The dashed vertical line is the Pe of the first flow. The smallest measureable stress difference in the frequency sweep measurements would correspond to approximately twice the error bar value or $\sim$0.1 Pa.

At first glance these results suggest that there is a significant anisotropic response due to the shear induced string structure. However, close examination of the stress amplitude response curves shows that the response along the orthogonal direction displays the same Pe_2 dependence as the quiescent sample where no first flow was applied. These results demonstrate that the significantly denser packing fraction along the orthogonal direction due to the string structure (Fig. 2(g)) dose not enhance the suspension stress response during the orthogonal modulation. Furthermore, the data for the parallel modulation (blue diamonds) are well fit by the eqn (2) for an isotropic suspension indicating that the string structure does not further affect the rheology. In fact, the suspension's response to parallel modulation appears to be dominated by hydrodynamic contributions that are relatively insensitive to the suspension structure (Fig 5). Finally, if the difference between the parallel and orthogonal stress responses was related to the string structure, we would have expected that it would have persisted until the second flow was strong enough to alter the string structure. However, the data for both modulations begin to overlap at $Pe_2 \approx 200$, which is still an order of magnitude smaller than Pe_1. Thus we are forced to conclude that while the rheology of the string structure is anisotropic, this anisotropy does not result from the shear induced string structure.

5   Discussion and conclusion

Using a novel biaxial confocal rheoscope, we measured the rheological response of the vorticity-aligned string phase along the flow and vorticity directions. This apparatus enabled us to control the orientation and morphology of the sheared colloidal suspension under confinement. We showed that by varying the phase between the two shear directions the sample transitions from a string phase to an isotropic phase. By employing various biaxial shear protocols, we found that despite its anisotropic structure, the string phase rheology is quantitatively similar to that of the isotropic suspension for the range of frequencies and strain amplitudes explored. These result are in agreement with previous work that shows hydrodynamic interactions play a crucial role in the formation of the string phase and dominate its rheological response.[18] In addition, the measurements presented here demonstrate that for the tested volume fractions ($\phi = 0.37$ and 0.47) and degree of confinement, the hydrodynamic contribution to the shear stress is not significantly altered by the suspension microstructure. This structure-independent hydrodynamic response is reminiscent of the weak correlation between the structure and rheology in other complex fluids.[43,46] For instance, it was recently shown that layering in sheared suspensions of hard-sphere colloids does not correlate with any rheological signature.[43] As another example, the strong viscoelasticity of the synthetic clay Laponite does not depend on the fractal nature of its structure.[46] It is important to note that the viscosity under steady state conditions can be different from the reported amplitude of the complex viscosity under oscillatory shear. Therefore, it would be useful to conduct further experiments to investigate the

rheological anisotropy using a superposition of continuous and oscillatory shear.

In the frequency sweep measurements, we do find that suspensions demonstrate an anisotropic shear thinning behavior due to the applied first flow. This anisotropic shear thinning behavior in hard-sphere suspensions is remarkably different from the isotropic shear thinning observed in polymer solutions[34] and is an important result in itself. This thinning behavior is consistent with previous results that have demonstrated that as the system is driven towards high Pe or at a shear frequency above its relaxation rate, the Brownian stresses saturate and the overall viscosity decreases. The observed anisotropy in the stress response indicates that saturation of the Brownian stresses only occurs along the first flow direction. Our data show that such effects are sufficient to account for the measured anisotropic thinning behavior and that the added effect of the string structure is negligible.

In conclusion, by using oscillatory superposition spectroscopy, we find no measurable difference in the stress response between the isotropic and string phases. This finding implies that the hydrodynamically dominated high-frequency stress response model for the isotropic suspension can be applied to the confined anisotropic shear-induced structure reported here. Many studies conducted on other systems that also display vorticity-aligned strings suggest pronounced changes in the normal stress difference. It is interesting to ask whether such normal stress differences arise for the hard sphere system we study. Unfortunately, measurements of normal stress difference can not be performed with our current setup. Thus, this question remains unanswered. Nevertheless, the results presented here show that anisotropic structure does not always lead to a measurable anisotropic stress response at the frequency explored. Moreover, they illustrate a powerful approach for elucidating the underlying relationship between anisotropic structure and anisotropic rheology in systems driven far-from-equilibrium.

Appendix

Plate alignment and force measurement device calibration

To align the silicon wafer (top plate) and coverslip (bottom plate), after the sample is loaded in the shear cell we first use the confocal microscope to measure the gap height at the four corners and the center of the gap. Then, we finely adjust three differential screws on the shear cell to minimize the tilt of the top plate. After the differential screws are adjusted, we measure the gap height at the four corners and the center again to examine how parallel the plates are. We continuously perform this alignment process until two plates are aligned with less than $0.0075°$. Using the confocal microscope to measure the gap variation during alignment, we find the gap height variation across the plate to be less than 0.5 μm, which is close to the optical uncertainty along the vertical-axis (Y-axis) of the confocal microscope. We find that when there is a significant tilt between the two plates, or if one corner is lower than the others, we observe inhomogeneous shear flows. No such flows were observed in the experiments reported here.

To characterize the Force measurement device (FMD) performance, we measure the flow curve of a viscosity standard (VIS-RT5K-600, Paragon Scientific). With the given value of the fluid viscosity and the controlled shear rate, we are able to calculate the corresponding shear stress σ exerted on the FMD. We find linear relations between the applied shear stress and the FMD output signal over the range 0.05 Pa < σ < 2000 Pa for both axes, which determine the sensitivity (0.05 Pa) of the device Fig. 7. We also verify this calibration result by hanging weights off the FMD. This weight hanging method enables us to obtain the direct relation between the output signal of FMD and the applied force. We find that both calibrations are in excellent agreement with one another.

It is important to rule out the possibility that the measured shear stress is affected by other sources of force related to the capillary forces and deformation of the cover slip. To minimize the contribution of the capillary stress we overfill the sample so that the region within the shearzone is in contact with a suspension reservoir. Since the change in fluid boundary length in the reservoir is negligible during shear this force becomes small relative to the shear stress. By measuring the viscosity of simple fluids at various gap heights showing that they are purely viscous and indepenent of gap height, we are able to further rule out the effect of such capillary forces.[28] To determine the deformation of the coverslip we monitored the gap during our shear experiments. We find that the gaps remain constant to within our experimental resolution. We believe that this stability results from the high viscosity of the suspension solvent and the fact that our confocal imaging is conducted for a single height rather than a continuous 3D scan which may tug at the cover slip. Overall, we find that the biaxial FMD, our apparatus, and our experimental procedure allow for accurate measurement of the shear stress response of the suspension.

Acknowledgements

References

1 G. Yang, J. Kabel, B. Van Rietbergen, A. Odgaard, R. Huiskes and S. C. Cown, *J. Elasticity*, 1998, **53**, 125–146.

2 J. J. Hopfdeld, *J. Phys. Chem. Solids*, 1960, **15**, 97–107.

3 G. deWit and J. S. Koehler, *Phys. Rev.*, 1959, **116**, 11131120.

4 A. Rebhan and D. Steineder, *Phys. Rev. Lett.*, 2012, **108**, 021601.

5 J. Vermant and M. J. Solomon, *J. Phys.: Condens. Matter*, 2005, **17**, 187–216.

6 R. G. Larson, *The Structure and Rheology of Complex Fluids*, Oxford University Press, Oxford, 1998.

7 S. Hess, J. F. Schwarzl and D. Baalss, *J. Phys.: Condens. Matter*, 1990, **2**, SA279.

8 K. A. Kemp and S. V. Letcher, *Phys. Rev. Lett.*, 1971, **27**, 16341636.

9 A. Mertelj, A. Rešetič, S. Gyergyek, D. Makoveca and M. Čopič, *Soft Matter*, 2011, **7**, 125–131.

10 J. Gennisson, T. Deffieux, E. Mace, G. Montaldo, M. Fink and M. Tanter, *Ultrasound Med. Biol.*, 2010, **36**, 789801.

11 F. Pignon, A. Magnin and J. M. Piau, *Phys. Rev. Lett.*, 1997, **79**, 4689.

12 C. O. Osuji and D. A. Weitz, *Soft Matter*, 2008, **4**, 1388–1392.

13 A. Montesi, A. A. Pea and M. Pasquali, *Phys. Rev. Lett.*, 2004, **92**, 058303.

14 E. K. Hobbie, S. Lin-Gibson, H. Wang, J. A. Pathak and H. Kim, *Phys. Rev. E: Stat., Nonlinear, Soft Matter Phys.*, 2004, **69**, 061503.

15 V. Grenard, N. Taberlet and S. Manneville, *Soft Matter*, 2011, **7**, 3920–3928.

16 S. Lin-Gibson, J. A. Pathak, E. A. Grulke, H. Wang and E. K. Hobbie, *Phys. Rev. Lett.*, 2004, **92**, 048302.

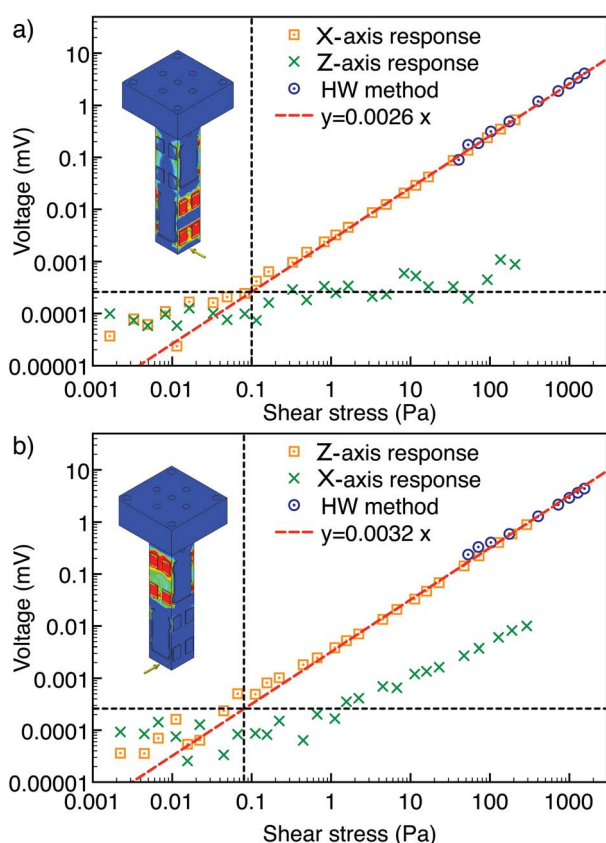17 B. Snook, E. Guazzelli and J. E. Butler, *Phys. Fluids*, 2012, **24**, 121702.

Fig. 7 The shear stress calibration with shear cell experiment and hanging weight method for *X*-axis (a) and *Z*-axis (b). The orange data are the response of the axis that is along the shear flow direction, and the green data represent the response of another axis. The blue data are the voltage response measured with the hanging weight method. The red curves are the linear fit to the data. The schematics of the strained force measurement device are generated by the finite element analysis.

18 X. Cheng, X. Xu, S. A. Rice, A. R. Dinner and I. Cohen, *Proc. Natl. Acad. Sci. U. S. A.*, 2011, **109**, 63–67.

19 M. Grzelczak, J. Vermant, E. M. Furst and L. M. Liz-Marzán, *ACS Nano*, 2010, **4**, 3591–3605.

20 P. Jiang and M. J. McFarland, *J. Am. Chem. Soc.*, 2004, **126**, 13778–13786.

21 J. Baudry, C. Rouzeau, C. Goubault, C. Robic, L. Cohen-Tannoudji, A. Koenig, E. Bertrand and J. Bibette, *Proc. Natl. Acad. Sci. U. S. A.*, 2006, **103**, 16076–16078.

22 R. Pasquino, F. Snijkers, N. Grizzuti and J. Vermant, *Rheol. Acta*, 2010, **49**, 993–1001.

23 L. B. Chen, B. J. Ackerson and C. F. Zukoski, *J. Rheol.*, 1994, **38**, 193–216.

24 B. J. Ackerson, *J. Rheol.*, 1990, **34**, 553–590.

25 R. Pasquino, F. Snijkers, N. Grizzuti and J. Vermant, *Langmuir*, 2010, **26**, 3016–3019.

26 H. M. Laun, R. Bung, K. Hahn, E. Hädicke, R. Hingmann, F. Schmidt, S. Hess, W. Loose, O. Hess and P. Lindner, *J. Rheol.*, 1992, **36**, 743–787.

27 K. M. Schmoller, P. Fernandez, R. C. Arevalo, D. L. Blair and A. R. Bausch, *Nat. Commun.*, 2010, **1**, 134.

28 X. Cheng, J. H. McCoy, J. N. Israelachvili and I. Cohen, *Science*, 2011, **333**, 1276–1279.

29 C. Gao, S. D. Kulkarni, J. F. Morris and J. F. Gilchrist, *Phys. Rev. E: Stat., Nonlinear, Soft Matter Phys.*, 2010, **81**, 041403.

30 R. Besseling, E. R. Weeks, A. B. Schofield and W. C. K. Poon, *Phys. Rev. Lett.*, 2007, **99**, 028301.

31 R. Besseling, L. Isa, P. Ballesta, G. Petekidis, M. E. Cates and W. C. K. Poon, *Phys. Rev. Lett.*, 2010, **105**, 268301.

32 C. Mobuchon, P. J. Carreau, M. Heuzey, N. K. Reddy and J. Vermant, *J. Rheol.*, 2009, **53**, 517.

33 J. W. Swan, R. Zia and J. F. Brady, *J. Rheol.*, 2014, **58**, 1.

34 J. Vermant, L. Walker, P. Moldenaers and J. Mewis, *J. Non-Newtonian Fluid Mech.*, 1998, **79**, 173–189.

35 J. Vermant, P. Moldenaers, J. Mewis, M. Ellis and R. Garritano, *Rev. Sci. Instrum.*, 1997, **68**, 4090–4096.

36 T. F. F. Farage and J. M. Brader, *J. Rheol.*, 2012, **56**, 259–278.

37 G. Ovarlez, Q. Barral and P. Coussot, *Nat. Mater.*, 2010, **9**, 115119.

38 L. Zou, *Phys. Rev. E: Stat., Nonlinear, Soft Matter Phys.*, 2010, **81**, 031302.

39 Z. Cheng, J. Zhu, P. M. Chaikin, S. Phan and W. B. Russel, *Phys. Rev. E: Stat., Nonlinear, Soft Matter Phys.*, 2002, **65**, 041405.

40 C. W. Macosko, *Rheology: Principles, Measurements, and Applications (Advances in Interfacial Engineering)*, Wiley-VCH, New York, 1994.

41 I. Sriram, E. M. Furst, R. J. DePuit and T. M. Squires, *J. Rheol.*, 2009, **53**, 357.

42 J. M. Brader, *J. Phys.: Condens. Matter*, 2010, **22**, 363101.

43 X. Xu, S. A. Rice and A. R. Dinner, *Proc. Natl. Acad. Sci. U. S. A.*, 2012, **110**, 3771–3776.

44 N. J. Wagner and J. F. Brady, *Phys. Today*, 2009, **62**, 27.

45 H. M. Laun, *Die Angewandte Makromolekulare Chemie*, 1984, **123**, 335.

46 D. Bonn, H. Kellay, H. Tanaka, G. Wegdam and J. Meunier, *Langmuir*, 1999, **15**, 75347536.